A&A 676, A48 (2023)
https://doi.org/10.1051/0004-6361/202346011

Astronomy & Astrophysics
Special issue

Solar Orbiter First Results (Nominal Mission Phase)

A high-latitude coronal mass ejection observed by a constellation of coronagraphs: Solar Orbiter/Metis, STEREO-A/COR2, and SOHO/LASCO

G. Zimbardo[1,⋆], B. Ying[2], G. Nisticò[1], L. Feng[2], L. Rodríguez-García[3], O. Panasenco[4], V. Andretta[5], D. Banerjee[6], A. Bemporad[7], Y. De Leo[8,9], L. Franci[10], F. Frassati[7], S. Habbal[11], D. Long[12,13], J. Magdalenic[14,15], S. Mancuso[7], G. Naletto[16], S. Perri[1], M. Romoli[17], D. Spadaro[18], M. Stangalini[19], L. Strachan[20], R. Susino[7], R. Vainio[21], M. Velli[22], C. M. S. Cohen[23], J. Giacalone[24], M. Shen[25], D. Telloni[7], L. Abbo[7], A. Burtovoi[26], G. Jerse[27], F. Landini[7], G. Nicolini[7], M. Pancrazzi[7], G. Russano[5], C. Sasso[5], and M. Uslenghi[28]

(Affiliations can be found after the references)

Received 28 January 2023 / Accepted 2 June 2023

ABSTRACT

Context. A few days before the first perihelion of the Solar Orbiter nominal mission, which occurred on 2022 March 26, the Metis coronagraph on board Solar Orbiter detected a coronal mass ejection (CME) that was moving away from the far side of the Sun (with respect to Solar Orbiter) at high northern latitudes. The eruption was also seen by other spacecraft, in particular, by STEREO-A, which was in quadrature configuration with Solar Orbiter.

Aims. We analyse the different views of the CME by a constellation of spacecraft with the purpose to determine the speed and acceleration of the CME, and to identify the source region of the CME.

Methods. Considering the positions of various spacecraft on 2022 March 22, this CME happened to be within the field of view of STEREO-A/SECCHI, and it was visible over the limb from SOHO/LASCO. We present the results of the 3D reconstruction of the CME based on the graduated cylindrical shell model and of the identification of the possible origin of the CME using extreme-ultraviolet (EUV) observations by Solar Orbiter/EUI, STEREO-A/EUVI, and SDO/AIA. The observations in EUV are compared with the coronal magnetic structure obtained by the potential field source surface method.

Results. The 3D reconstruction of the CME derives a central latitude of 29° N, a Stonyhurst longitude of −125°, and an average radial speed at the apex of $322 \pm 33\,\mathrm{km\,s^{-1}}$ between 4 and 13 $R_\odot$, which is probably not high enough to generate a shock wave. The estimated average acceleration of the CME is $16 \pm 11\,\mathrm{m\,s^{-2}}$ in the same range of distances from the Sun. This CME may be associated with the disappearance of a coronal cloud prominence, which is seen in the EUV by STEREO-A/EUVI and SDO/AIA, and is also associated with rapidly evolving emerging magnetic flux.

Key words. Sun: corona – Sun: coronal mass ejections (CMEs) – Sun: filaments, prominences – solar wind – Sun: UV radiation

1. Introduction

Coronal mass ejections (CMEs) are large eruptions of magnetized plasma that are expelled from the Sun into the heliosphere as a result of the release of the huge energy stored in the solar magnetic field structures. CMEs moving faster than the expanding corona can develop shock waves when the speed difference is larger than the fast magnetosonic speed (e.g. Bemporad & Mancuso 2010; Bemporad et al. 2014). CME-driven shock waves can convert the energy of ordered motion into thermal energy, and accelerate particles to energies exceeding several MeV (e.g. Lee et al. 2012; Rouillard et al. 2016; Rodríguez-García et al. 2021). Furthermore, even CMEs that are not very fast in the solar corona can lead to strong magnetic disturbances in the geospace environment, as occurred for one of the strongest geomagnetic storms of solar cycle 24 (Gopalswamy et al. 2022). Therefore, it is important to understand the origin, speed, and acceleration of CMEs. Remote-sensing observations of CMEs close to the Sun provide evidence of the existence of magnetic flux-rope (MFR) structures within CMEs (Vourlidas 2014). The 3D MFR geometry in terms of CME propagation direction, orientation, width, and speed can be derived from the imaging observations from multiple vantage points to minimize projection effects using forward modelling, such as the graduated cylindrical shell (GCS) model (Thernisien et al. 2006; Thernisien 2011). Farther out from the Sun, CMEs interact with the solar wind in a complex way that depends on the properties of fast and slow solar wind streams (Rodríguez-García et al. 2022); this can lead to deformations of the initial CME structure, including also concave CME shapes (Savani et al. 2010; Yang et al. 2023).

The Solar Orbiter spacecraft is equipped with a complete suite of instruments to explore the solar environment and the inner heliosphere (Müller 2020; Zouganelis et al. 2020). On 2022 March 26, Solar Orbiter attained its first perihelion of the nominal phase mission, reaching a heliocentric distance as close as 0.32 au. This allowed an unprecedented view of the solar environment. During this perihelion, the Metis coronagraph on board Solar Orbiter (Antonucci et al. 2020; Romoli et al. 2021) gathered a large number of high-resolution images of an already active corona during the rising phase of the solar cycle. In particular, a few days before the perihelion, namely starting at 19:27 UT on 2022 March 22, Metis detected a neat CME that apparently emerged from the north pole, as shown in Fig. 1, but that propagated from the far side of the Sun with respect to Solar Orbiter at high northern latitudes, as verified by inspection of data from other spacecraft.

⋆ Also an INAF associate.

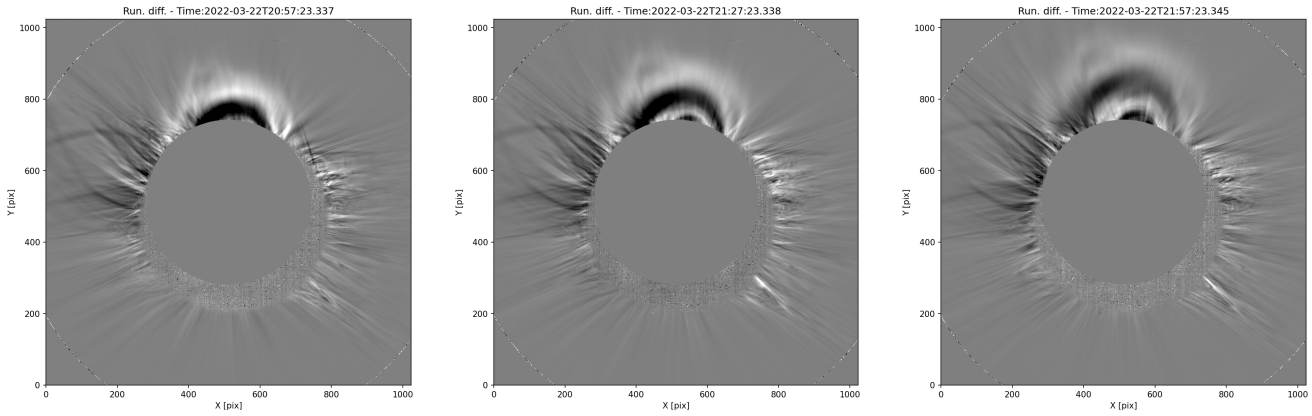

Fig. 1. Visible-light running-difference images of the CME observed by Metis. The times of each snapshot are indicated at the top of each panel.

In this paper, we use observations of three coronagraphs, namely Metis on board Solar Orbiter, COR2 on board the ahead spacecraft from the twin Solar TErrestrial RElations Observatory (STEREO-A; Kaiser et al. 2008), and the Large Angle and Spectrometric COronagraph (LASCO; Brueckner et al. 1995) on board the SOlar and Heliographic Observatory (SOHO; Domingo et al. 1995), to carry out the 3D reconstruction of the CME.

We deduce the kinematics of the CME, such as its speed and acceleration, via the 3D reconstruction to determine the acceleration mechanism of the CME. Furthermore, we investigate the possible origin of the CME by means of extreme-ultraviolet (EUV) observations of the low corona. The structures seen in the EUV as part of a coronal cloud prominence are compared with the magnetic structure obtained by the potential field source surface (PFSS; Schrijver & De Rosa 2003) method for 2022 March 22.

The paper is organized as follows. In Sect. 2 we present the coronagraphic observations of the CME. Section 3 shows the 3D reconstruction of the CME for heliocentric distances between ~3 and ~14 $R_\odot$. The uncertainities on the parameters of the reconstruction are considered, and the CME speed and acceleration are derived. The high quality of Metis images also provides clues regarding the density structure of the solar corona at ~2 $R_\odot$. In Sect. 4 we search for the possible origin of the CME using EUV observations of the low corona and a comparison with the magnetic pressure map obtained from PFSS. Finally, Sect. 5 summarizes the main conclusions of this study and discusses the acceleration mechanism and the possible presence of a CME-driven shock and energetic particles.

2. Coronagraphic observations of the 2022 March 22 coronal mass ejection

During March 2022, several other spacecraft in addition to Solar Orbiter observed the Sun remotely. In particular, STEREO-A was in nearly exact quadrature with Solar Orbiter, with a longitudinal separation of 85.6° between the two spacecraft, and it was able to observe the March 22 CME in its plane of sky. This can be considered one of the few CMEs that are observed in quadrature from Solar Orbiter and another spacecraft so far. Moreover, SOHO, located at ~52° from Solar Orbiter, was able to observe this CME clearly. The CME was soon in the field of view of LASCO, having originated beyond the east solar limb as seen from SOHO. The positions of the various spacecraft are shown in Fig. 2, where we also show coronagraphic images of the CME taken from different points of view at slightly different times, namely 22:27 UT for Metis, 22:24 UT for LASCO, and 22:08 UT for COR2. Therefore, a stereoscopic view of the CME is available, which allows a reliable 3D reconstruction (Balmaceda et al. 2018). We note that COR2 images between 19:38 UT and 22:03 UT are missing. Images from LASCO C2 and C3 are available with a high cadence. They are useful to fill the gap in COR2 data and to obtain images when the CME was beyond the Metis field of view.

Figure 2 shows that no spacecraft was on the opposite side of Solar Orbiter to make in situ measurements of the interplanetary CME (Jian et al. 2006). The coronal activity associated with the evolving CME has been detected by the Wide-field Imager for Parker Solar PRobe (WISPR) heliospheric imager (Vourlidas et al. 2016) on board the Parker Solar Probe (PSP; Fox et al. 2016; see Sect. 4).

3. 3D reconstruction of the coronal mass ejection

In this section, we show the results of the 3D reconstruction of the CME using the GCS model. The GCS model is an empirical model built to combine self-similar expansion and flux-rope morphology, consisting of two conical legs, with the cone apices connected to the Sun's centre, and a torus connecting the legs (Thernisien et al. 2006; Thernisien 2011). It can be used to estimate the physical parameters of the CME, including its position, direction, and true speed. Six geometric parameters are required, namely the central latitude θ and central longitude ϕ of the CME apex, the axial tilt γ, which is the angle of the main axis of the CME with respect to the solar equator, the height of the apex $h_{\rm front}$ (or equivalently, the height of the conical legs $h_{\rm leg}$), the half-angle α, which is half the angular distance between the conical leg axes, and the aspect ratio κ, which is the sine of the opening angle of the cones, as shown in Fig. 1 of Thernisien (2011). These parameters are used to fit the CME shape to compare with the visually projected image of the CME in coronagraphs from different perspectives, as explained in Thernisien et al. (2009). From now on, when we discuss the results of the GCS forward fitting method, we simply refer to it as a 3D reconstruction of the CME shape.

The CME was reconstructed by combining the information obtained by the LASCO C2 and Metis coronagraphs before 22:00 UT (an example is shown in Fig. 3 at about 20:27 UT, when the CME was still in the low corona) and by including LASCO C3 and COR2 after 22:24 UT. The CME was only reconstructed from three perspectives at around 22:27 UT, as

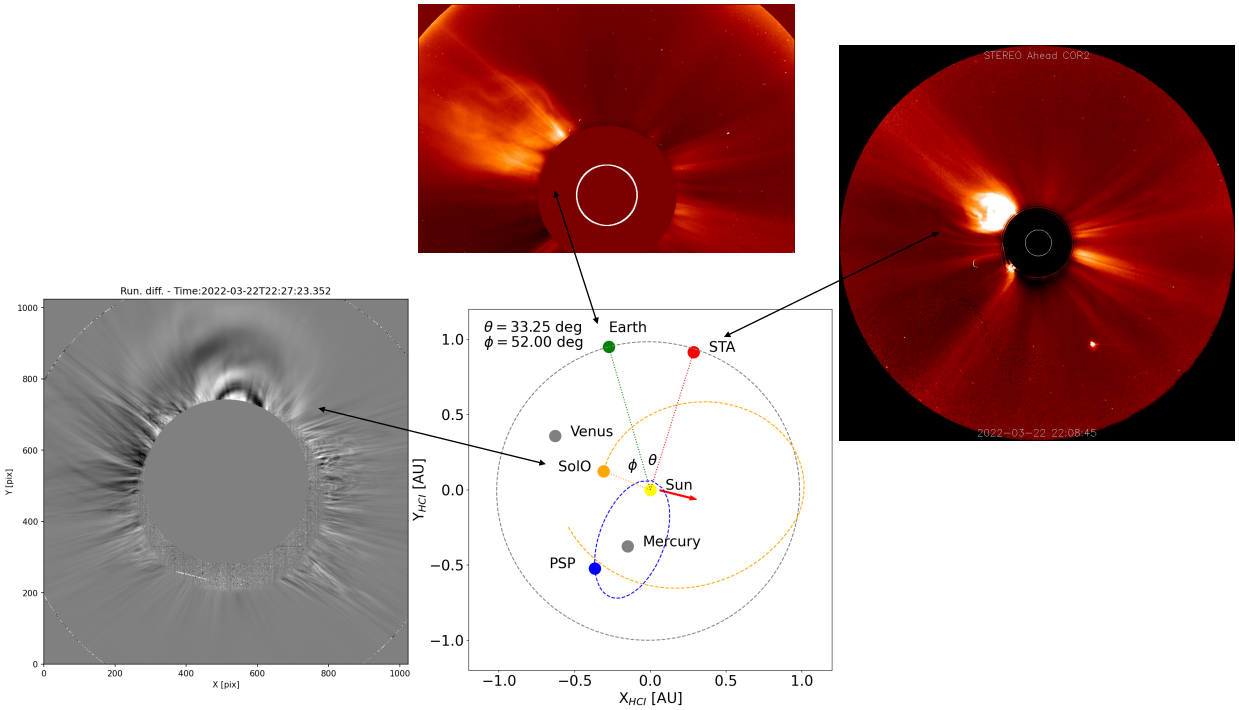

Fig. 2. Spacecraft positions on 2022 March 22 (lower centre panel): Solar Orbiter (SolO), the Parker Solar Probe (PSP), and STEREO-A (STA). Also, SOHO and the Solar Dynamics Observatory are located close to the Earth. The direction of propagation of the CME apex, projected onto the ecliptic plane, is shown by the red arrow. The coronagraphic images show the CME as seen at similar times by Metis (lower left panel), LASCO-C2 (upper centre panel), and COR2 (upper right panel).

shown in Fig. 4. The reconstruction at a later time, 01:38 UT on March 23, is shown in Fig. 5. The full set of fitting parameters from the GCS model was used to determine the CME front position, speed, and acceleration, as discussed below. For this event, based on the fitting procedure, we find that the half-angle is zero, implying that the CME is similar to an ice-cream cone model (Fisher & Munro 1984; Thernisien 2011). We note that the GCS model with zero half-angle was used by Patsourakos et al. (2010) to fit a CME in the low corona, using both STEREO-A and STEREO-B coronagraphic and EUV images. The GCS model parameters for all available times are given in Table 1, except for the tilt angle, which is unnecessary when $\alpha = 0$. The values of these parameters are subject to uncertainty, as given in Table 2 of Thernisien et al. (2009). In a recent study by Verbeke et al. (2023), the errors were quantified by comparing synthetic data obtained by ray-tracing and magnetohydrodynamic simulations with the GCS reconstruction performed from several different viewpoints. They reported that the errors substantially decrease from a reconstruction based on one viewpoint to two viewpoints, while the errors do not decrease significantly when three viewpoints are used that are all in the ecliptic plane. Their estimates of the minimum error bars for the CME parameters are $\Delta\theta \simeq 6°$ (latitude), $\Delta\phi \simeq 11°$ (longitude), $\Delta\gamma \simeq 25°$ (tilt), $\Delta\alpha \simeq 10°$ (half-angle), $\Delta h \simeq 0.6\,R_\odot$ (height), and $\Delta\kappa \simeq 0.1$ (ratio). Since our fits were carried out with either two or three viewpoints, these values can be considered as the typical uncertainties of the parameters reported in Table 1.

During the CME propagation, the average aspect ratio is $\kappa \sim 0.38$. The CME central latitude is $\sim 29°$ N, and the Stonyhurst longitude is $\sim -125°$. The longitude of Solar Orbiter was 52.4°, and therefore, longitudinal separation between Solar Orbiter and the CME is 177.4°, which shows that the CME was almost fully on the far side of the Sun as seen from Solar Orbiter. The CME propagated in the plane of sky of COR2. Because the projection effects are small, this is advantageous for determining the CME speed and latitude.

Table 1 shows that the model parameters change only slightly with time, in agreement with the assumption of self-similar expansion. This property is supported by a recent numerical simulation that reported that CMEs expand in a self-similar way, without significant changes of shape, up to about $30\,R_\odot$ (Yang et al. 2023). We note that the GCS reconstruction for the studied event is very accurate, as shown by the comparison of the top and bottom panels in Figs. 3 and 4, even for the cases when one of the coronagraphs, namely Metis, was at a substantially smaller heliospheric distance, 0.32 au, than the other spacecraft. Conversely, Fig. 5 shows that the reconstruction only captures the large-scale features of the CME, but not the details. A latitudinal asymmetry of the CME is clearly seen in the upper left panel of Fig. 5, which can also be seen at earlier times, as observed by STEREO-A in Fig. 2.

The parameters of the GCS reconstruction can be used to create synthetic images of the CME by simulating the brightness of the visible light radiation subject to Thomson scattering. We used a tool that is based on the raytracing software available in SolarSoftWare (Freeland & Handy 1998) and adapted to PSP/WISPR observations by Nisticò et al. (2020). For our purposes, the tool was re-adapted to Solar Orbiter in order to create synthetic observations in white light of the Metis coronagraph. Figure 6 shows a sample of the synthetic images of the CME structure observed on March 22 at two different times. The shape of the CME is prescribed by the GCS model, but a thin shell of the electron density at the surface of the model is imposed in order to simulate the Thomson-scattered radiation. The left panels show the CME projected in the solar equatorial plane, and the right panels present the plane-of-sky as seen by Metis. For

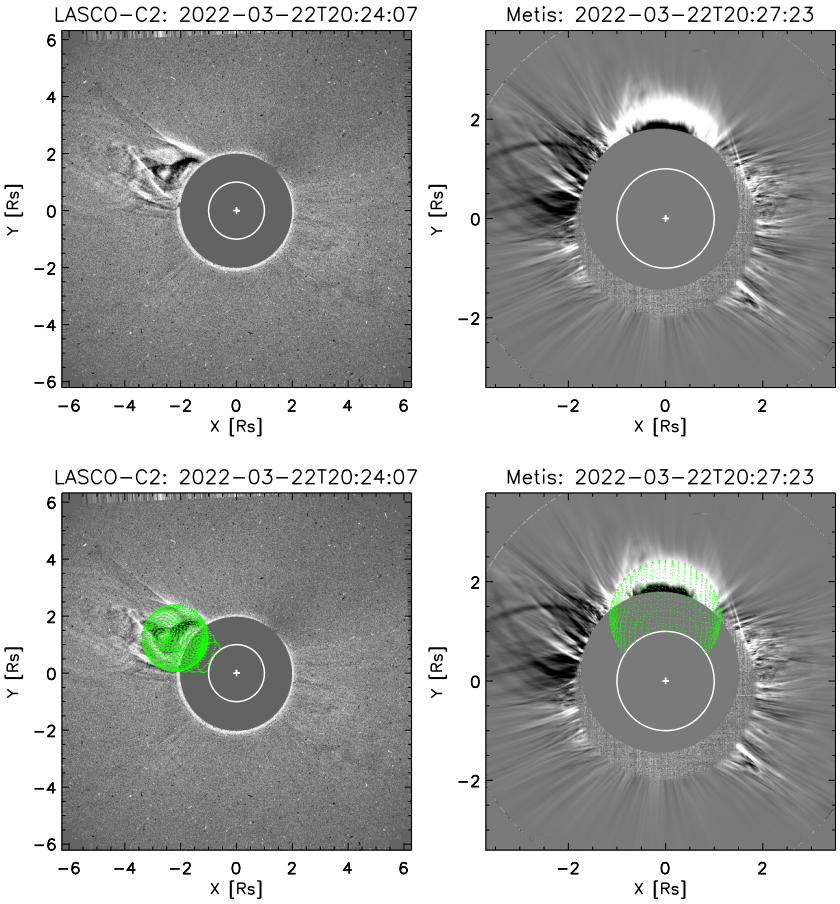

Fig. 3. 3D reconstruction of the CME using LASCO-C2 (left panels) and Metis (right panels). The times of each image are indicated at the top of each panel. The top (bottom) panels show the coronagraph images without (with) the reconstructed structure, which is shown by the green mesh.

the purpose of this work, we did not compare the brightness profiles of the synthetic CME with the observed profile, but simply achieved a qualitative comparison of the CME morphology. We note bright loop structures in the CME in the synthetic images, similar to what was observed in the running-difference images from Metis. This structuring might be caused by the integration of the radiation along the line of sight of different portions of the CME body that are located at different scattering angles. We aim at studying the brightness profiles of the CME in a future work in more depth.

The LASCO observation panels of Fig. 3 and especially Fig. 4 show that the CME exhibits considerable helical structure (e.g. Antonucci et al. 1997; Ciaravella et al. 2000). The temporary rotation associated with untwisting can be deduced from Metis images: The arched structures above the north pole in the upper right panel of Fig. 4 are more pronounced on the left side and less pronounced on the right side. Because these are running-difference images, this implies that the left side receded faster than the right side, that is, as seen from the CME footpoint, the rotation would be counterclockwise.

When the different sizes of the fields of view are taken into account, the comparison of the coronagraphic images in Figs. 3 and 4 allows us to appreciate the high spatial resolution of Metis, which unveils very fine radial structures in the corona at about 2 solar radii. Visible-light images are due to the scattering of photospheric light by free electrons in the corona. These radial structures therefore correspond to magnetic flux tubes with different plasma densities. This is reminiscent of the very fine and elongated magnetic flux tubes that are visible during total solar eclipses. A quantitative estimate of the local electron density values and gradient scale has been carried out by Nisticò et al. (2022), by means of the passage of comet Lovejoy in the low corona. Metis observations are an important complement to local density determinations and show that the fine density structuring of the solar corona is a common feature. This density structure can have important implications for the dissipation of low-frequency waves in the corona because a variable density causes variations in the local Alfvén speed, leading to a distortion of wave fronts (e.g. Malara 2013).

The CME front kinematics is presented in Fig. 7. The average speed derived from a linear fit between 3.85 $R_\odot$ and 13.21 $R_\odot$ is 322 ± 33 km s^{-1}, and it is shown by the dashed line in Fig. 7. We assumed an error bar on the front distance of ±1 $R_\odot$, which is higher than the minimum value of ±0.6 $R_\odot$ proposed by Verbeke et al. (2023). An increase in the CME front speed with solar distance can be observed from the data points, in agreement with previous studies (e.g. Patsourakos et al. 2010; Bein et al. 2011). A quadratic fit, indicated by the dotted line in Fig. 7, yields an initial speed at 19:57 UT of 165 ± 118 km s^{-1} and an acceleration of 16 ± 11 m s^{-2}. The final speed at 01:38 UT on March 23 is about 480 km s^{-1}. The moderate initial speed at a height of 3.85 $R_\odot$ is consistent with a CME origin from a coronal cloud prominence, as shown in Fig. 8 and discussed in Sect. 4.

4. Origin of the coronal mass ejection

The coronagraphic observations of Metis, COR2, and LASCO were combined with the extreme-ultraviolet observations at 304 Å from the Extreme Ultraviolet Imager (EUVI; Wuelser et al. 2004) on board STEREO-A and at 171 Å from the Atmospheric Imaging Assembly (AIA; Lemen et al. 2012) on board the Solar Dynamics Observatory (SDO; Pesnell et al. 2012) in order to study the

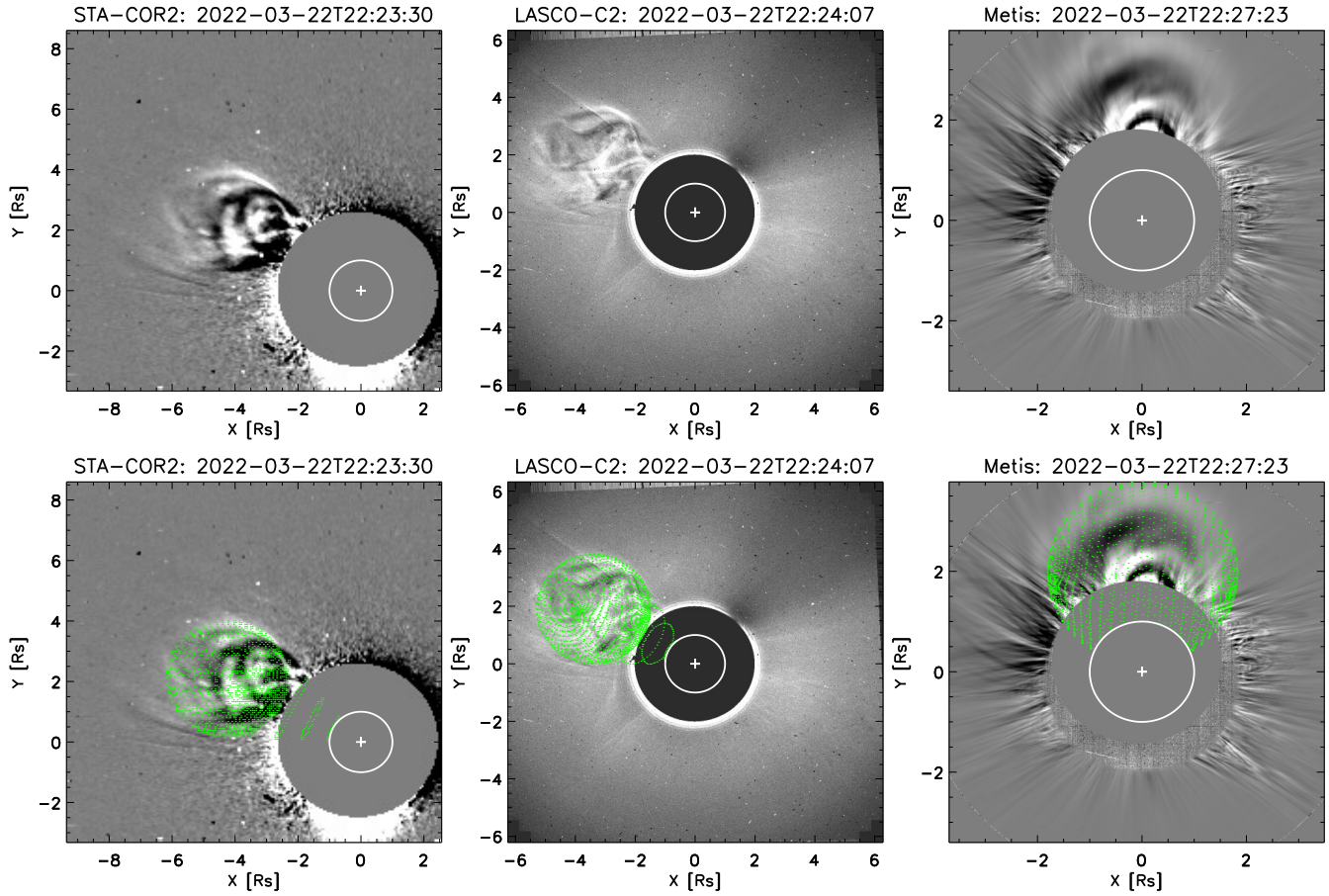

Fig. 4. 3D reconstruction using COR2 (left), LASCO-C2 (centre), and Metis (right). The times of each image are indicated at the top of each panel. The top (bottom) panels show the coronagraph images without (with) the reconstructed structure, which is shown by the green mesh. The comparison of the three coronagraphic images allows us to appreciate the high spatial resolution of Metis, which unveils very fine density structures in the corona.

coronal activity near the source region of the CME. The CME was almost in the plane of the sky of STEREO-A, and, as observed by STEREO-A, there were substantial activities in the northern east limb, such as a coronal cloud prominence formation and coronal rain (Panasenco et al. 2019), frequent flares, and loop arcades at least three days before the CME emergence. We found clues for the identification of the CME source by extrapolating the CME initial speed, assumed constant for simplicity, down to the low corona. We estimated that the prominence in Fig. 8 is located at a height of $\sim$1.4 $R_\odot$, so that the time to reach 3.85 $R_\odot$ moving at $\sim$165 km s^{-1} is about 2 h and 52 min. This implies a starting time close to 17:05 UT, which matches the time of the prominence destabilization reasonably well.

Figure 8 shows that a coronal cloud prominence (Panasenco et al. 2019) forms above the region from which the CME is likely to have come. The STEREO-A/EUVI images at 304 Å show this coronal cloud prominence and the corresponding plasma downflow (coronal rain) along a few threads starting on 2022 March 19 at 16:05 UT, when it became visible above the eastern limb from the STEREO-A point of view and continued until the magnetic funnel supporting this cloud evolved. The low part of this coronal cloud prominence has been observed at times very close to those of EUVI by SDO/AIA at hotter coronal temperatures in 171 Å as well (Fig. 8, bottom panels). In order to emphasise the prominence, in comparison to the background corona, we increased the constrast in Fig. 8. We note that the signal was particularly weak in 171Å, which implies that the coronal threads observed at this wavelength have temperatures below one million degrees. The arched structure visible at 16:05 UT opens up at 18:05 UT (left and right panels of Fig. 8, respectively) both in the EUVI and AIA images, and it is the most likely low coronal signature of the observed CME. The plane of sky of STEREO-A/EUVI (Stonyhurst longitude 33.25° + 90° E, Fig. 2) is very close to the longitude of the GCS reconstruction central longitude (Stonyhurst longitude 125° E, Table 1), and the GCS reconstruction central latitude (28° N, Table 1) matches the latitude of the left leg of the arched structure well. Solar Orbiter/EUI detected some of the cloud prominence shown in Fig. 8 at around 14:50 UT–16:00 UT (not shown), even though the prominence was on the far side from Solar Orbiter. This can be attributed to the fact that coronal cloud prominences form relatively high in the corona.

We consider that the plasma sources for the 2022 March 19–22 prominence were the continuous flaring activity caused by newly emerging and evolving active regions and the multiple CMEs originating from the same area, which is outlined by the dashed blue rectangle in Fig. 9. During the period of 2022 March 19–22, this area produced at least six CMEs, including the CME we study in this paper. As observed by SOHO/LASCO-C2, they are (1) a faint, slow, small CME on March 19, ~06:00 UT; (2) a large CME on March 20, ~10:40 UT; (3) a faint, fast, small CME on March 20, ~17:30 UT; (4) a small, faint CME on March 21, ~20:10 UT; (5) a very slow, faint, large CME on March 22, ~07:00 UT; and (6) the CME under study on March 22,

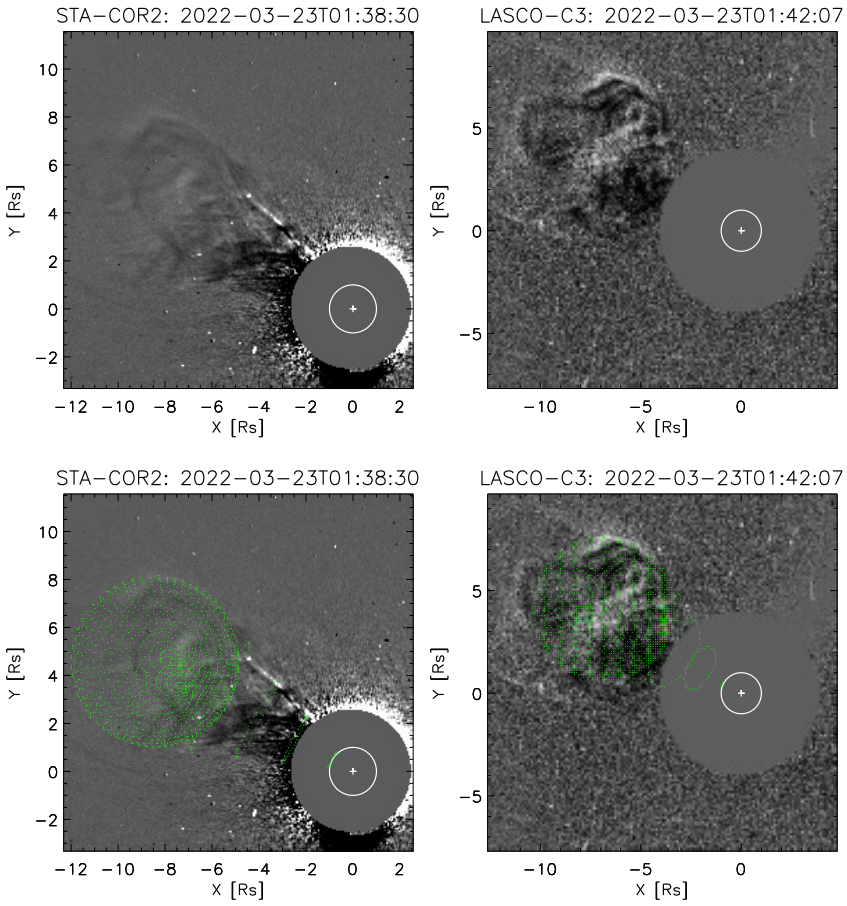

Fig. 5. 3D reconstruction using COR2 (left panels) and LASCO-C3 (right panels). The times of each image are indicated at the top of each panel. The top (bottom) panels show the coronagraph images without (with) the reconstructed structure, which is shown by the green mesh.

Table 1. GCS model parameters.

Date	Time (UT)			$h_{\rm front}$ ($R_\odot$)	$h_{\rm leg}$ ($R_\odot$)	ϕ (deg)	θ (deg)	κ	α (deg)
	COR2	LASCO	Metis						
2022 March 22	–	20:00:07	19:57:23	3.857	2.384	–125.42	27.95	0.382	0.0
2022 March 22	–	20:24:07	20:27:23	4.284	2.648	–125.51	27.95	0.382	0.0
2022 March 22	–	21:24:07	21:27:23	5.358	3.410	–124.60	27.95	0.364	0.0
2022 March 22	–	22:00:07	21:57:23	6.072	3.696	–124.70	27.95	0.391	0.0
2022 March 22	22:23:30	22:24:07	22:27:23	6.714	4.005	–125.16	28.04	0.404	0.0
2022 March 22	23:07:45	23:06:15	–	8.000	4.895	–124.80	29.52	0.388	0.0
2022 March 22	23:38:30	23:42:07	–	8.929	5.518	–124.51	29.62	0.382	0.0
2022 March 22	23:53:30	23:54:07	–	9.500	5.959	–124.38	30.18	0.373	0.0
2022 March 23	00:38:30	00:42:07	–	11.072	6.944	–123.76	30.18	0.373	0.0
2022 March 23	00:53:30	00:54:09	–	11.600	7.276	–123.63	30.18	0.373	0.0
2022 March 23	01:38:30	01:42:07	–	13.214	8.288	–123.21	30.18	0.373	0.0

Notes. The columns show from left to right the day of observations, the observational time by COR2, LASCO, Metis, the height of the CME front apex, the height of conical legs, the Stonyhurst longitude, the Stonyhurst latitude, the aspect ratio, and the half-angle between the conical legs.

~19:00 UT. We also note that the PSP was located almost on the opposite side of STEREO-A, as shown in Fig. 2, with the WISPR field of view looking towards the right of the Sun. Inspection of WISPR Level 1 images for the period of 2022 March 22 (not shown) shows multiple broad density structures propagating in the middle northern latitudes several hours before the CME emergence, starting at around 13:00 UT and lasting up to 24:00 UT and beyond. These early structures were ejected a few hours before the CME studied here, and they are not directly related to it. Instead, they are associated with one of the preceding slow CMEs that was first seen in the LASCO-C2 field of view at ~07:00 UT on March 22. However, the structures observed later than 20:00 UT could correspond to the propagating CME we focus on here. The presence of preceding CMEs is relevant for the origin of our CME because some percentage of the erupting plasma of any CME falls back into the corona. When a magnetic structure is nearby, such as a large-scale magnetic funnel, a coronal cloud will form.

Figure 9 shows the magnetic pressure map at a height of 1.2 $R_\odot$ for the period corresponding to the CME formation. A solid thick black line shows the model neutral line at 1.2 $R_\odot$, and black contours indicate the magnetic field pressure at 1.2 $R_\odot$. The

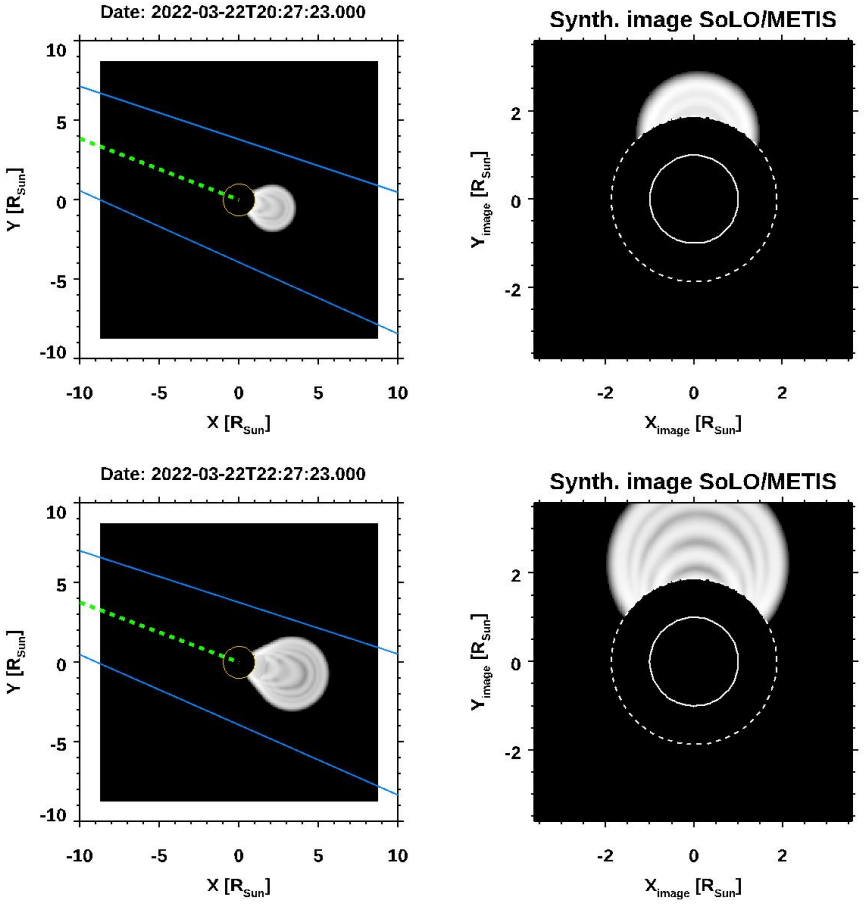

Fig. 6. Synthetic images of the CME obtained by ray-tracing based on the GCS reconstruction parameters for two times corresponding to Fig. 3 (top) and to Fig. 4 (bottom). The left panels show the 3D reconstruction projected onto the solar equatorial plane: the dashed green line represents the Solar Orbiter look direction, and the blue lines delimit the Metis field of view. The right panels show the synthetic images corresponding to the Metis point of view.

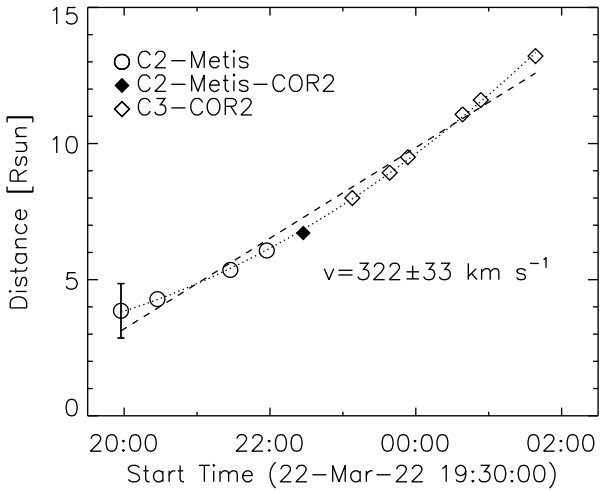

Fig. 7. Radial distance from the Sun centre of the CME front, obtained by the 3D reconstruction, as a function of time. The different symbols indicate the instruments that were used, as shown in the legend. The average speed for the whole period is obtained by a linear fit, which is indicated by the dashed line. The CME front acceleration is obtained by a quadratic fit, which is indicated by the dotted line (details are given in the main text). The error bar, corresponding to $\pm 1\,R_\odot$ for all points, is shown only for the first data point to allow a better visual inspection of the fitting.

mapping uses the potential field source surface (PFSS) model by Schrijver & De Rosa (2003). As a lower boundary condition, the PFSS model incorporates magnetic field maps produced by an evolving surface-flux transport model based on magnetic fields observed by the Helioseismic and Magnetic Imager (HMI; Scherrer et al. 2012; Schou et al. 2012) on the SDO. The PFSS model has proved to be rather accurate during early PSP orbits due to the low level of solar activity (Bale et al. 2019; Panasenco et al. 2020). In Fig. 9 we project the origin area of the reconstructed CME at a selected time of 22:27 UT, when the CME was in the field of view of all the coronagraphs (Fig. 4), onto the PFSS magnetic pressure contour map and outline it by a dashed blue rectangle. Inside the rectangle in Fig. 9 lie two rapidly evolving active regions with sunspots, a negative open magnetic field area (blue shade), and solid black neutral lines. The part of the neutral line between 10° and 50° Carrington longitude may be associated with the CME because it encompasses the −125° Stonyhurst longitude, corresponding to 31° Carrington longitude obtained by the GCS modeling, as shown in Table 1, and the EUV flaring regions shown in Fig. 8. The newly emerging magnetic flux and evolving active region westward of this neutral line cause the coronal magnetic field reconfiguration, and probably triggered the CME. A cross section of the magnetic field structure obtained by the PFSS model, at 15° latitude and inside the area outlined by the blue-dashed rectangle, is shown in Fig. 10. A magnetic funnel is visible in the area in which the cloud prominence was observed. To show the magnetic funnel more clearly, the image in Fig. 10 has been rotated northward of ∼75°.

5. Summary and discussion

We reported observations of a high-latitude CME observed by a constellation of coronagraphs, close to the Solar Orbiter perihelion on 2022 March 26. The CME was seen in quadrature

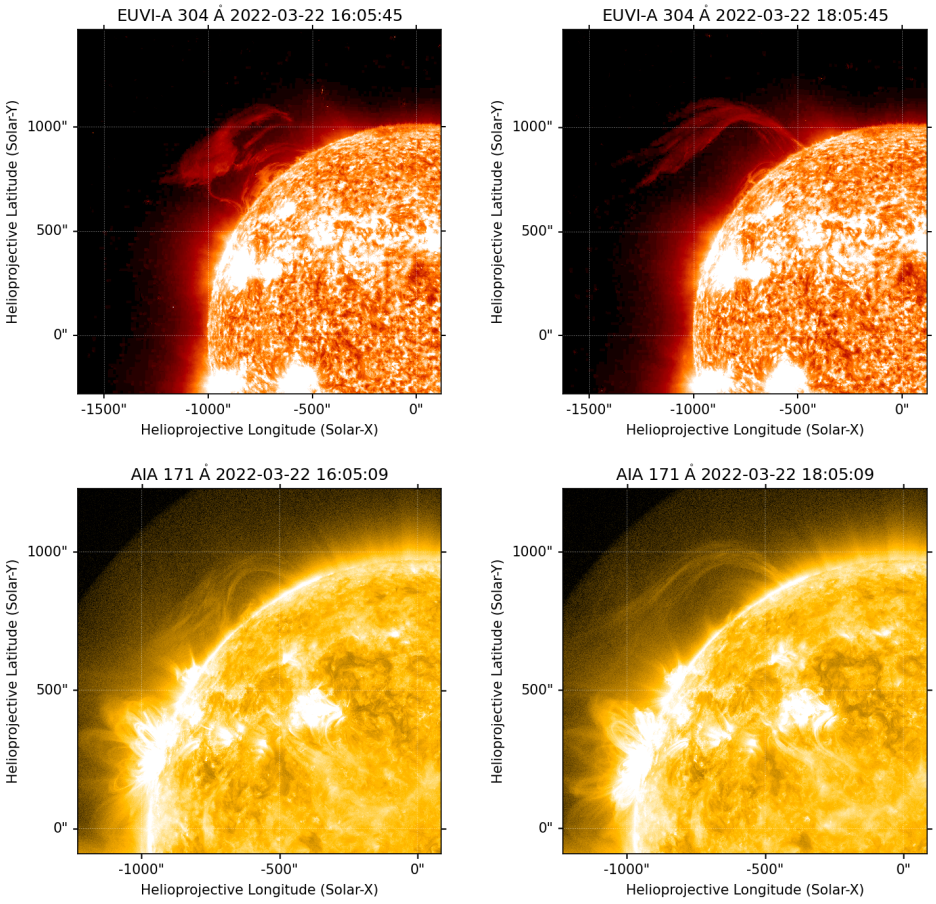

Fig. 8. EUV images of the Sun obtained by STEREO-A, which was in quadrature with Solar Orbiter, and by SDO, which was separated by 52° in longitude from Solar Orbiter. Upper panels: Sun as seen in the 304 Å line by STEREO-A/EUVI, a few hours before the CME rise. Lower panels: Sun as seen in the 171 Å line by SDO/AIA at about the same times. Arched and dynamic coronal cloud prominence downflows are seen near and above of the source region of the CME.

by the coronagraphs on board Solar Orbiter and STEREO-A, when the longitudinal separation between the two spacecraft was ∼86°. The Metis coronagraph on board Solar Orbiter (Stonyhurst longitude of 52.4°) detected a coronal mass ejection at around 19:57 UT on 2022 March 22, which apparently emerged from the north polar region and travelled away from the far side of the Sun with respect to Solar Orbiter. In addition, this CME was well within the fields of view of STEREO-A/SECCHI (longitude of −33.2°) and of SOHO/LASCO. The availability of several points of view allowed the 3D reconstruction of the CME, which was carried out with the graduated cylindrical shell model. The 3D reconstruction gives a central Stonyhurst longitude of ∼−125°, a central latitude of ∼29° N, and a half-angle equal to zero, implying that the CME corresponds to the ice-cream cone model; the average aspect ratio is 0.38. The reconstruction yields a CME average radial speed of ∼320 ± 30 km s^{-1} and an average acceleration of 16 ± 11 m s^{-2}. Since STEREO-A was in quadrature with Solar Orbiter, it was able to observe the source region of the CME in its plane of sky. In particular, EUV observations by STEREO-A/EUVI and SDO/AIA indicate that the CME is associated with the opening up of an arched magnetic structure and the destabilisation of a coronal cloud prominence. Inspection of the magnetic pressure map and of the magnetic field line structure obtained by a PFSS model suggests that the coronal cloud was supported by a magnetic funnel configuration before destabilisation. Unfortunately, it was not possible to follow the evolution of the interplanetary CME in situ because no spacecraft was located along the CME path.

Figure 7 shows that the quadratic fit for the CME acceleration is very accurate, which implies a nearly constant acceleration rate for more than five hours. This feature should be explained by the acceleration mechanisms. Current models include acceleration by magnetic reconnection below the erupting CME and by the Lorentz force acting on the electric current flowing inside the CME flux rope (e.g. Sachdeva et al. 2017). The acceleration value, 16 ± 11 m s^{-2}, is an order of magnitude higher than the values reported by Gopalswamy et al. (2000), which were obtained for the entire transit from the Sun to near Earth, however. Instead, the obtained acceleration is at the lower end of the range of values reported by Bein et al. (2011), who considered a set of 95 CMEs in the low corona. Strong acceleration in the low corona was reported by Temmer et al. (2010) as well. Our acceleration value is close to the acceleration values, about 10 m s^{-2}, in the corona at heights of 6−24 $R_\odot$ reported for the CME of 2013 February 27 by Zhuang et al. (2022). In the latter case, prolonged magnetic reconnection in the source region of the CME was suggested as the cause of the CME acceleration. Magnetic reconnection was also suggested to power the acceleration of about 10 m s^{-2} of the CME on 2018 August 20, which originated from an erupting filament and lasted for radial distances larger than 50 $R_\odot$ (Gopalswamy et al. 2022). The magnetic breakout model (Antiochos et al. 1999), which encompasses magnetic reconnection above a multipolar magnetic structure, is able to cause fast CME acceleration, but it can also give a constant acceleration rate for several hours, as well as speed and acceleration values similar to ours (Lynch et al. 2004; Karpen et al. 2012). We suggest that magnetic reconnection causes the acceleration for the present CME because of the moderate values of speed and acceleration, the presence of a neutral line in the dashed blue rectangular area in Fig. 9, and the likely erupting prominence origin of the CME. Conversely, Bein et al. (2011) reported that strong, impulsive

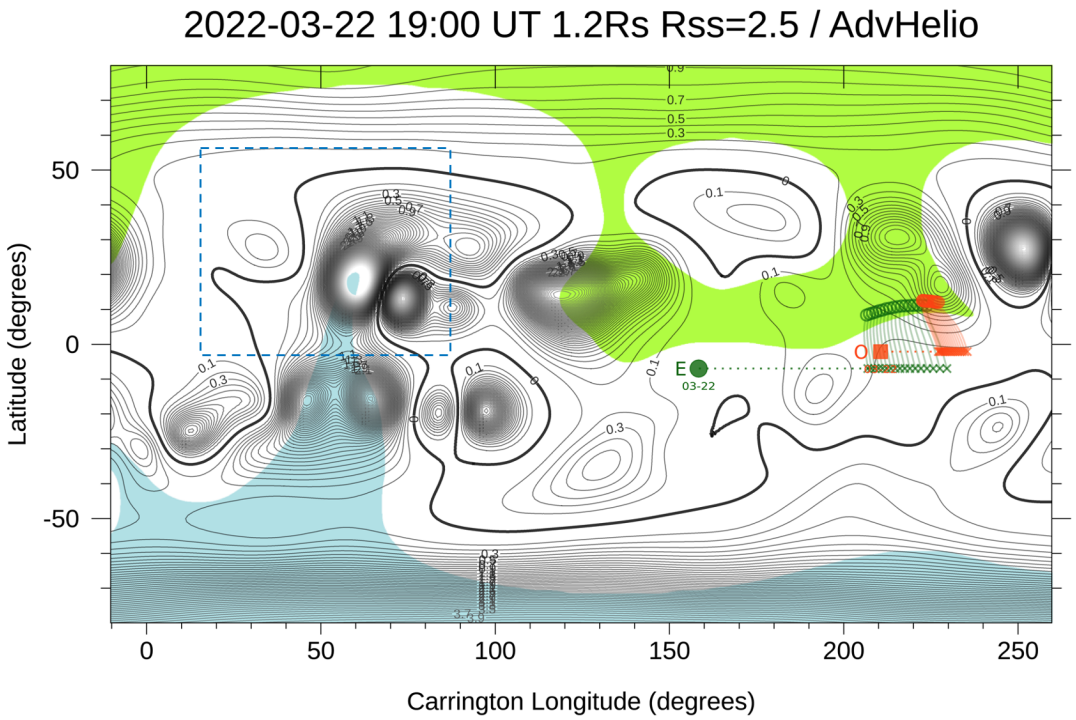

Fig. 9. Magnetic pressure (B^2) contour map for 2022 March 22 based on the SDO/HMI magnetograms. The region from which the CME of March 22 originated is outlined by the dashed blue rectangular between 10 Å and 90 Å Carrington longitude. A PFSS model maps the magnetic connection of Earth (E) and Solar Orbiter (O) from the source surface (SS) at 2.5 $R_\odot$ to a height of 1.2 $R_\odot$ above the photosphere. The solid black lines show the model neutral lines at 1.2 $R_\odot$. Black contours indicate the magnetic field pressure at 1.2 $R_\odot$ (~140 Mm). The ballistic projection of the positions of Earth (green circle) and Solar Orbiter (red square) on the SS (crosses) and down to the solar wind source regions (circles) are calculated for the height $R = 1.2\,R_\odot$ and the in situ measured solar wind speed ±80 km s^{-1}. Open magnetic field regions are shown in blue (negative) and green (positive). The area inside the dashed blue rectangular contains strong magnetic field regions, a negative open magnetic field area (sky blue), and two sections of a neutral line, one of which may be the CME source.

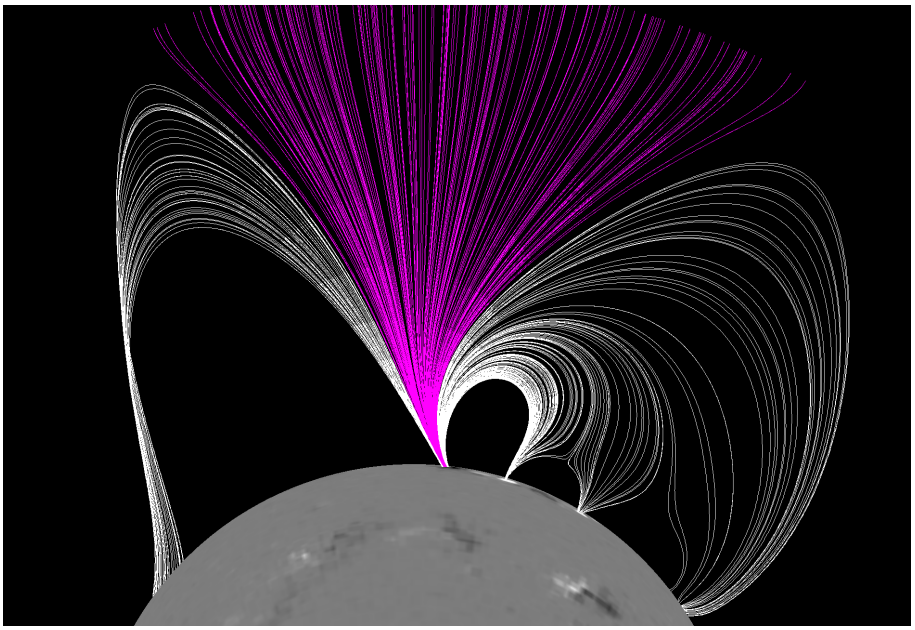

Fig. 10. Funnel magnetic configurations of open field lines (purple). Magnetic field lines are obtained from a PFSS slice taken across the area above which the coronal cloud prominence formed on 2022 March 21. The image has been rotated northward to give a better view of the magnetic funnel.

acceleration in the low corona can be explained by the Lorentz force. In addition, MHD waves may have a relevant role in the evolution of prominences, leading to the loss of vertical stability (Kolotkov et al. 2016, 2018).

Coronal mass ejections often drive shock waves, but no shock front can easily be detected in our images. In order to understand whether this CME may have driven a shock, we can compare the CME speed with some available determinations of the coronal outflow speed. In particular, we can refer to observations carried out by Cranmer et al. (1999) with the SOHO Ultra-Violet Coronagraph Spectrometer (UVCS; Kohl et al. 1995) of the hydrogen outflow velocity over coronal holes at solar

minimum determined by Doppler dimming. Cranmer et al. (1999) found outflow velocities of ~280 km s^{-1} for a proton parallel (with respect to the magnetic field) temperature equal to the electron temperature, and of ~400 km s^{-1} for isotropic proton temperature, at a radial distance of 4 $R_\odot$. Similar values were obtained by Cranmer (2020) by using a Monte Carlo simulation of the Ly-α profiles. A detailed study of the outflow velocity during June 1997 (i.e. during solar minimum) between 1.5 and 4 $R_\odot$ and as a function of heliographic latitude was carried out by Dolei et al. (2018): at 4 $R_\odot$, the outflow speed varied from about 150 km s^{-1} at equatorial latitudes to about 400 km s^{-1} at polar latitudes. A further estimate has been obtained by Metis on 2020 May 15 by means of the Ly-α H$_I$ UV observations (Romoli et al. 2021). With the caution due to the fact that the coronal configuration in March 2022 is rather different from that in May 2020, which was in the solar minimum, Metis obtained coronal velocity maps that show an outflow velocity between 180 and 220 km s^{-1} at radial distances of 5−6 $R_\odot$ in the regions on the plane of the sky within the range ±0.7 $R_\odot$ from the equatorial plasma layer. The CME of March 22 clearly propagated at high latitudes, away from the streamer belt. Assuming that the above determinations of the outflow velocity are also indicative of the coronal speed before our event, a CME speed of less than 300 km s^{-1} at distances of 4−6 $R_\odot$ (shown in Fig. 7) is probably not high enough to generate a shock in a plasma outflow, which arguably has speeds of about 300 km s^{-1} or more. Another indication of coronal shocks is the observation of strong type II radio bursts (Bemporad & Mancuso 2010). We checked radio observations, in particular, STEREO-A/WAVES (Bougeret et al. 2008) measurements for March 22[1], and also ground-based observations by e-CALLISTO and other observatories that were observing at the time of the CME. No indication of radio bursts is found in the WAVES dataset, even though this could be due to the fact that the radio emission beam did not intercept STEREO-A. In summary, the absence of a shock front in the coronagraphs, the low CME speed, and the absence of a radio burst indicate that no shock was formed.

We also searched for energetic particle signatures in the Energetic Particle Detector (EPD; Rodríguez-Pacheco et al. 2020) on board Solar Orbiter and in the Integrated Science Investigation of the Sun (IS⊙IS; McComas et al. 2016) suite on board the PSP. Considering the positions of various spacecraft on 2022 March 22 (Fig. 2), assuming a nominal Parker spiral and the CME longitudinal width of about 60°, we can infer that PSP could be reasonably well connected to the event early on (except for possible latitudinal issues), and should be able to observe the energetic particles associated with the CME, if any, propagating along the spiral magnetic field. However, both the observations of the EPD instrument on Solar Orbiter and the IS⊙IS instrument on PSP showed no energetic particle signature in association with this CME (not shown). For Solar Orbiter, the lack of energetic particles can be due to the large angular separation between the CME location and Solar Orbiter magnetic footpoint. For PSP, the lack of energetic particle features associated with the CME could be due to the slow CME speed and the absence of a shock able to accelerate particles. However, for both spacecraft, the increase in energetic particles could be hidden because of the background of a previous event on March 21 (Pacheco et al., in prep.).

Finally, we point out that the possibility of having a stereoscopic view of a coronal event such as this CME on the far side from Solar Orbiter is related to the availability of a constellation of coronagraphs at several heliographic longitudes. These studies will greatly benefit from the Advanced Space-based Solar Observatory (ASO-S) Chinese spacecraft (Gan et al. 2019), launched on 2022 October 9, and carrying the Lyman-α Solar Telescope (LST) instrument (Li et al. 2019; Feng et al. 2019), which can image the Sun and the inner corona with a field of view up to 2.5 solar radii in both white light and the H$_I$ Ly-α line; and from the forthcoming launch of the Aditya-L1 spacecraft, carrying the Visible Emission Line coronagraph (VELC; Raghavendra Prasad et al. 2017). Aditya -L1 is going to be the first observatory-class solar space mission of India, and is expected to be launched in the first half of 2023. In addition, a new boost to multi-point solar observations will be attained when Solar Orbiter will begin to increase the inclination of its orbit above the ecliptic plane and reach new observing vantage points.

Acknowledgements. Solar Orbiter is a space mission of international collaboration between ESA and NASA, operated by ESA. Metis was built and operated with funding from the Italian Space Agency (ASI), under contracts to the National Institute of Astrophysics (INAF) and industrial partners. Metis was built with hardware contributions from Germany (Bundesministerium für Wirtschaft und Energie through DLR), from the Czech Republic (PRODEX) and from ESA. The Metis team thanks the former PI, Ester Antonucci, for leading the development of Metis until the final delivery to ESA. We would like to thank the whole Solar Orbiter community for realizing this exciting mission. This work is the outcome of the activities of Metis topical team TT9 – Coronal Shocks and Particle Acceleration. We thank A. Vourlidas for interesting discussions. G.N. acknowledges the Rita Levi Montalcini 2017 fellowship funded by the Italian Ministry of Research. D.M.L. is grateful to the Science Technology and Facilities Council for the award of an Ernest Rutherford Fellowship (ST/R003246/1). L.R.-G. acknowledges the financial support by the Spanish Ministerio de Ciencia, Innovación y Universidades FEDER/MCIU/AEI Projects ESP2017-88436-R and PID2019-104863RB-I00/AEI/10.13039/501100011033 and by the European Union's Horizon 2020 research and innovation program under grant agreement No. 101004159 (SERPENTINE). J.M. acknowledges funding by the BRAIN-be project SWiM (Solar Wind Modeling with EUHFORIA for the new heliospheric missions). O.P. was supported by the NASA grant No. 80NSSC20K1829. L.S. was supported by NASA through IAT # NNH12AT20I to NRL. G.Z. and S.P. acknowledge support from the Italian Space Agency (ASI) and the National Institute of Astrophysics (INAF), in the framework of the CAESAR (Comprehensive Space Weather Studies for the ASPIS prototype realization) project, through the ASI-INAF n. 2020-35-HH.O agreement for the development of the ASI Space weather Infrastructure (ASPIS) prototype of scientific data centre for Space Weather. Also, G.Z. has been partially supported in the framework of the contract ARG-IT-PRP-G-ESA-220003D for the Phase A/B study of the HENON mission of the ASI Alcor program.

References

Antiochos, S. K., DeVore, C. R., & Klimchuk, J. A. 1999, ApJ, 510, 485
Antonucci, E., Kohl, J. L., Noci, G., et al. 1997, ApJ, 490, L183
Antonucci, E., Romoli, M., Andretta, V., et al. 2020, A&A, 642, A10
Bale, S. D., Badman, S. T., Bonnell, J. W., et al. 2019, Nature, 576, 237
Balmaceda, L. A., Vourlidas, A., Stenborg, G., & Dal Lago, A. 2018, ApJ, 863, 57
Bein, B. M., Berkebile-Stoiser, S., Veronig, A. M., et al. 2011, ApJ, 738, 191
Bemporad, A., & Mancuso, S. 2010, ApJ, 720, 130
Bemporad, A., Susino, R., & Lapenta, G. 2014, ApJ, 784, 102
Bougeret, J. L., Goetz, K., Kaiser, M. L., et al. 2008, Space Sci. Rev., 136, 487
Brueckner, G. E., Howard, R. A., Koomen, M. J., et al. 1995, Sol. Phys., 162, 357
Ciaravella, A., Raymond, J. C., Thompson, B. J., et al. 2000, ApJ, 529, 575
Cranmer, S. R. 2020, ApJ, 900, 105
Cranmer, S. R., Kohl, J. L., Noci, G., et al. 1999, ApJ, 511, 481
Dolei, S., Susino, R., Sasso, C., et al. 2018, A&A, 612, A84
Domingo, V., Fleck, B., & Poland, A. I. 1995, Sol. Phys., 162, 1
Feng, L., Li, H., Chen, B., et al. 2019, RAA, 19, 162
Fisher, R. R., & Munro, R. H. 1984, ApJ, 280, 428
Fox, N. J., Velli, M. C., Bale, S. D., et al. 2016, Space Sci. Rev., 204, 7
Freeland, S. L., & Handy, B. N. 1998, Sol. Phys., 182, 497
Gan, W.-Q., Zhu, C., Deng, Y.-Y., et al. 2019, RAA, 19, 156

[1] https://secchirh.obspm.fr

Gopalswamy, N., Lara, A., Lepping, R. P., et al. 2000, Geophys. Res. Lett., 27, 145
Gopalswamy, N., Yashiro, S., Akiyama, S., et al. 2022, J. Geophys. Res.: Space Phys., 127, e30404
Jian, L., Russell, C. T., Luhmann, J. G., & Skoug, R. M. 2006, Sol. Phys., 239, 393
Kaiser, M. L., Kucera, T. A., Davila, J. M., et al. 2008, Space Sci. Rev., 136, 5
Karpen, J. T., Antiochos, S. K., & DeVore, C. R. 2012, ApJ, 760, 81
Kohl, J. L., Esser, R., Gardner, L. D., et al. 1995, Sol. Phys., 162, 313
Kolotkov, D. Y., Nisticò, G., & Nakariakov, V. M. 2016, A&A, 590, A120
Kolotkov, D. Y., Nisticò, G., Rowlands, G., & Nakariakov, V. M. 2018, J. Atmos. Solar-Terres. Phys., 172, 40
Lee, M. A., Mewaldt, R. A., & Giacalone, J. 2012, Space Sci. Rev., 173, 247
Lemen, J. R., Title, A. M., Akin, D. J., et al. 2012, Sol. Phys., 275, 17
Li, H., Chen, B., Feng, L., et al. 2019, RAA, 19, 158
Lynch, B. J., Antiochos, S. K., MacNeice, P. J., Zurbuchen, T. H., & Fisk, L. A. 2004, ApJ, 617, 589
Malara, F. 2013, A&A, 549, A54
McComas, D. J., Alexander, N., Angold, N., et al. 2016, Space Sci. Rev., 204, 187
Müller, D., St. Cyr, O. C., Zouganelis, I., , et al. 2020, A&A, 642, A1
Nisticò, G., Bothmer, V., Vourlidas, A., et al. 2020, Sol. Phys., 295, 63
Nisticò, G., Zimbardo, G., Perri, S., et al. 2022, ApJ, 938, 20
Panasenco, O., Velli, M., & Panasenco, A. 2019, ApJ, 873, 25
Panasenco, O., Velli, M., D'Amicis, R., et al. 2020, ApJS, 246, 54
Patsourakos, S., Vourlidas, A., & Kliem, B. 2010, A&A, 522, A100
Pesnell, W. D., Thompson, B. J., & Chamberlin, P. C. 2012, Sol. Phys., 275, 3
Raghavendra Prasad, B., Banerjee, D., & Singh, J. 2017, Curr. Sci., 113, 613
Rodríguez-García, L., Gómez-Herrero, R., Zouganelis, I., et al. 2021, A&A, 653, A137
Rodríguez-García, L., Nieves-Chinchilla, T., Gómez-Herrero, R., et al. 2022, A&A, 662, A45
Rodríguez-Pacheco, J., Wimmer-Schweingruber, R. F., Mason, G. M., et al. 2020, A&A, 642, A7
Romoli, M., Antonucci, E., Andretta, V., et al. 2021, A&A, 656, A32
Rouillard, A. P., Plotnikov, I., Pinto, R. F., et al. 2016, ApJ, 833, 45
Sachdeva, N., Subramanian, P., Vourlidas, A., & Bothmer, V. 2017, Sol. Phys., 292, 118
Savani, N. P., Owens, M. J., Rouillard, A. P., Forsyth, R. J., & Davies, J. A. 2010, ApJ, 714, L128
Scherrer, P. H., Schou, J., Bush, R. I., et al. 2012, Sol. Phys., 275, 207
Schou, J., Scherrer, P. H., Bush, R. I., et al. 2012, Sol. Phys., 275, 229
Schrijver, C. J., & De Rosa, M. L. 2003, Sol. Phys., 212, 165
Temmer, M., Veronig, A. M., Kontar, E. P., Krucker, S., & Vršnak, B. 2010, ApJ, 712, 1410
Thernisien, A. 2011, ApJS, 194, 33
Thernisien, A. F. R., Howard, R. A., & Vourlidas, A. 2006, ApJ, 652, 763
Thernisien, A., Vourlidas, A., & Howard, R. A. 2009, Sol. Phys., 256, 111
Verbeke, C., Mays, M. L., Kay, C., et al. 2023, Adv. Space Res., in press [arXiv:2302.00531]
Vourlidas, A. 2014, Plasma Phys. Control. Fusion, 56, 064001
Vourlidas, A., Howard, R. A., Plunkett, S. P., et al. 2016, Space Sci. Rev., 204, 83
Wuelser, J. P., Lemen, J. R., Tarbell, T. D., et al. 2004, SPIE Conf. Ser., 5171, 111
Yang, L., Hou, C., Feng, X., et al. 2023, ApJ, 942, 65
Zhuang, B., Lugaz, N., Temmer, M., Gou, T., & Al-Haddad, N. 2022, ApJ, 933, 169
Zouganelis, I., De Groof, A., Walsh, A. P., et al. 2020, A&A, 642, A3

[1] University of Calabria, Physics Department, Ponte P. Bucci, Cubo 31 C, Rende, Italy
e-mail: gaetano.zimbardo@fis.unical.it
[2] Purple Mountain Observatory, Chinese Academy of Sciences, Nanjing 210023, PR China
[3] Universidad de Alcalá, Space Research Group, Alcalá de Henares, 28801 Madrid, Spain
[4] Advanced Heliophysics Inc., Pasadena, CA, USA
[5] INAF – Capodimonte Astronomical Observatory, Salita Moiariello 16, 80131 Naples, Italy
[6] Aryabhatta Research Institute of Observational Sciences, India
[7] INAF – Turin Astrophysical Observatory, Via Osservatorio 20, 10025 Pino Torinese, TO, Italy
[8] University of Catania – Physics and Astronomy Department "Ettore Majorana", Via Santa Sofia 64, 95123 Catania, Italy
[9] Max-Planck-Institut für Sonnensystemforschung, Justus-von-Liebig-Weg 3, 37077 Göttingen, Germany
[10] School of Physical and Chemical Sciences, Queen Mary University of London, London, UK
[11] Institute for Astronomy, University of Hawaii, Honolulu, HI 96822, USA
[12] University College London, Mullard Space Science Laboratory, Holmbury St. Mary, Dorking, Surrey RH5 6NT, UK
[13] Astrophysics Research Centre, School of Mathematics and Physics, Queen's University Belfast, University Road, Belfast BT7 1NN, UK
[14] SIDC, Royal Observatory of Belgium, Brussels, Belgium
[15] Center for Mathematical Plasma Astrophysics, Department of Mathematics, KU Leuven, Celestijnenlaan 200B, 3001 Leuven, Belgium
[16] University of Padova – Physics and Astronomy Department "Galileo Galilei", Via F. Marzolo 8, 35131 Padua, Italy
[17] University of Florence – Physics and Astronomy Department, Via Sansone 1, 50019 Sesto Fiorentino, FI, Italy
[18] INAF – Catania Astrophysical Observatory, Via Santa Sofia 78, 95123 Catania, Italy
[19] Agenzia Spaziale Italiana, Via del Politecnico, 00133 Rome, Italy
[20] Naval Research Laboratory, 4555 Overlook Ave. SW, Washington, DC 20375, USA
[21] Department of Physics and Astronomy, University of Turku, 20014 Turku, Finland
[22] Department of Earth, Planetary, and Space Sciences, University of California, Los Angeles, CA 90095, USA
[23] California Institute of Technology, Pasadena, CA 91125, USA
[24] University of Arizona, Tucson, AZ 85721, USA
[25] Department of Astrophysical Sciences, Princeton University, Princeton, NJ, USA
[26] INAF – Osservatorio Astrofisico di Arcetri, Largo Enrico Fermi 5, 50125 Florence, Italy
[27] INAF, Astronomical Observatory of Trieste, Località Basovizza 302, 34149 Trieste, Italy
[28] INAF, Institute of Space Astrophysics and Cosmic Physics of Milan, Via Alfonso Corti 12, 20133 Milano, Italy